Topics in Catalysis
https://doi.org/10.1007/s11244-023-01780-0

ORIGINAL PAPER

Tracking Structural Deactivation of H-Ferrierite Zeolite Catalyst During MTH with XRD

Izar Capel Berdiell[1] · Giorgio Bruno Braghin[1,2] · Tomás Cordero-Lanzac[1] · Pablo Beato[3] · Lars F. Lundegaard[3] · David Wragg[1,4] · Silvia Bordiga[2] · Stian Svelle[1]

Accepted: 4 January 2023

Abstract
We used the methanol-to-hydrocarbon (MTH) reaction as a shape-selective model reaction to investigate coke formation in zeolite H-Ferrierite. Despite being a 2D topology in terms of channel propagation, the FER framework displays a lattice expansion in all three dimensions of space upon deactivation. Therefore, the volume of the unit cell is an excellent X-Ray diffraction (XRD) descriptor for the catalyst deactivation. A model with dummy atoms added, also proved to be an accurate approach to measure the amount of internal coke and/or water inside the pore network correlated with thermogravimetric analysis results. While the catalyst deactivation of the H-Ferrerite during the MTH was fast, a comparably long induction period was observed. We were able to track such fast deactivation with the aforementioned descriptors by means of an *operando* XRD study by a standard laboratory diffractometer.

Keywords MTH · Deactivation · Coke · H-Ferrierite · XRD · Operando

1 Introduction

Zeolites are porous materials widely used towards a wide range of industrial applications. These materials are based on silicon-aluminium oxide tetrahedral units and can be classified by the size of their porous channels which is commonly referred by the amount of tetrahedral units (T atoms).

H-Ferrierite (FER) is one of the "big five" zeolites, in the sense that it is one of the most industrially applied materials [1]. It has an orthorhombic small and medium pore structure. The maximum symmetry of the topology is described by the *Immm* space group, which enforces 180° T-O-T angle between the "rigid walls". Relaxation of these angles was proposed with a monoclinic structure [2], but it can be also accounted with the orthorhombic *Pnnm* space group [3]. Such model has channels that propagate in the crystallographic *a* and *b* directions (Fig. 1). The *c* direction has no large pore system, and its rigid walls explain why the material tends to grow as platelets that are easily exfoliated [4].

H-Ferrierite has been used as a high-olefin cracking catalyst [5], in the dehydration of methanol for dimethyl ether (DME) synthesis [6] and skeletal isomerization of n-butenes to isobutene [7, 8], where the improvement of mass transport limitation dramatically enhanced the catalyst lifetime and process efficiency [9]. Other applications of FER framework include transition metals loading that resulted in materials used as passive NO_x adsorbers [10, 11] or in methane to methanol partial oxidation [12]. In general, the main cause of deactivation of catalytic processes with organic reactants in acid zeolites is the formation of coke; bulky organic species that cannot diffuse through the channel network blocking the pores of the zeolite [13]. The methanol-to-hydrocarbons (MTH) chemistry is known to follow the so-called dual cycle autocatalytic mechanism [14]. In the early stages of the mechanism (induction period), methanol forms a hydrocarbon pool that later on forms the hydrocarbons that diffuse out of the zeolite channels. Once the steady-state autocatalytic cycle is ongoing,

✉ Izar Capel Berdiell
izarc@uio.no

[1] Department of Chemistry, Center for Materials Science and Nanotechnology (SMN), University of Oslo, Blindern, P.O. Box 1033, 0315 Oslo, Norway

[2] Department of Chemistry, INSTM Reference Center and NIS Interdepartmental Center, University of Turin, Via Giuria 7, 10135 Turin, Italy

[3] Topsoe A/S, Haldor Topsøes Allé 1, 2800 Kgs. Lyngby, Denmark

[4] Institute for Energy Technology, Instituttveien 18, 2007 Kjeller, Norway

Published online: 19 January 2023

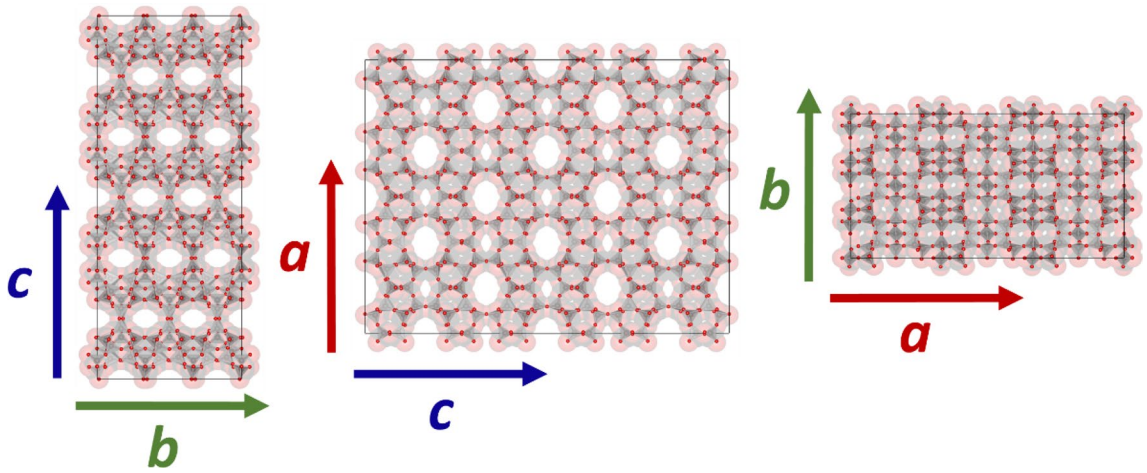

Fig. 1 Representation of H-Ferrierite topology. 10T (medium) and 8T (small) pore channels across *b* and *a* directions respectively. Note that these are the crystallographic planes of *Pnnm*, differently defined in the *Immm* model

different reaction pathways occurs in the alkene and aromatic cycle: methylation, dealkylation, oligomerization, cracking, hydrogen transfer and cyclization reactions. But the presence of aromatic intermediates also lead to condensation reactions towards bulky polyaromatics that causes catalyst deactivation. Studies of the MTH reaction at different temperatures using H-Ferrierite have shown a long induction period at the beginning of the reaction and a significantly fast drop of the activity [15]. This work also demonstrated the important role of aromatics intermediates in the evolution of the different mechanism, including the role and growth of aromatics inside pores.

In a previous work, we demonstrated the potential of X-Ray diffraction (XRD) to monitor changes in the zeolite framework caused by the formation of this aromatic intermediates within the zeolite cavities [16]. XRD can therefore be used to both track the status of the catalyst and the progress of the reaction in time resolved *operando* experiments [17, 18] as previously demonstrated for several zeotype catalysts [19]. Due to the particularity of MTH reaction evolution over time on stream, H-Ferrerite is a good candidate to explore the evolution of the catalyst status during the induction and deactivation period. In this work, XRD has been used to track FER framework during MTH reaction using both ex-situ and *operando* conditions. The evolution of framework changes has been correlated with the composition of the gas phase and the status of the catalyst (surface area and amount of coke) at different stages of the reaction.

2 Experimental Section

2.1 Catalyst Deactivation

The catalytic reactions were performed at atmospheric pressure in a fixed-bed quartz reactor with the catalyst powder pressed and sieved to 250–420 µm. The inner diameter of the reactor was 6 mm. The reaction temperature was monitored by a thermocouple protected by a 3 mm wide quartz sleeve inserted into the middle of the catalyst layer. For each experimental run, the reactor was loaded with 162–200 mg of catalyst. Prior to the reaction, the catalyst was activated with an initial heating ramp of 10 °C/min under 20% O_2 in nitrogen to 550 °C, and the temperature was kept for 1 h under O_2. Then, the catalytic bed was cooled to reaction temperature under argon atmosphere. The deactivation of the H-Ferrierite zeolite took place at 307 mbar of partial pressure of methanol (MeOH) at 400 °C balanced with helium (purity 5.0). The total flow was 13.8–17 ml/min (4.24–5.22 ml/min MeOH and 9.56–11.8 ml/min helium), giving a space velocity of 2 $g_{MeOH}/g_{catalyst}$ h. The partial pressure of MeOH was controlled with a condenser set at 37 °C. The effluent from the reactor was analyzed after 2 min of the start of the reaction and subsequently every 62.5 min by an on-line GC–MS analyzer (Agilent 7890A with flame ionization

detector and Agilent 5975C mass spectrometer) by using two Restek Rtx-DHA-150 columns. Hydrogen (Praxair, purity 6.0) was used as the carrier gas.

2.2 Basic Catalyst Characterization

Adsorption properties of the materials were evaluated by nitrogen adsorption–desorption measurements performed at the nitrogen boiling point (− 196 °C) on a Bel Belsorp-mini II instrument. Before the measurements, the samples were pretreated under vacuum for 1 h at 80 °C and then for 3 h more at 300 °C. Surface area values were calculated using the BET equation. The particle size was investigated by scanning electron microscopy (SEM) on a Hitachi SU 8230 FE-SEM instrument with a field emission gun operated at 1 kV. The fresh zeolite samples were fixed on aluminum stubs with double-sided carbon tape. For structural analysis, fresh and deactivated samples were placed in 0.7 mm open glass capillaries; XRD on the hydrated form was collected before the water was removed by heating at 200 °C for 2 h and flame sealing the capillaries. X-ray diffractograms were recorded at 25 °C using a Bruker D8-A25 in transmission capillary geometry with Ge (111) Johanssen monochromator and Lynxeye detector with Cu K-alpha-1 radiation ($\lambda = 1.5406$). The amount of coke species in the catalysts was quantified by thermogravimetric analysis (TGA) on a Netzsch STA 449 TG. Approximately 18 mg of catalyst was heated under 25 ml/min of synthetic air to 800 °C at a rate of 10 °C/min. Total mass loss is assigned to coke burning plus water removal. The total amount of coke is given in wt% relative to dried catalyst (mass at 300 °C in the TGA profiles).

2.3 Operando Powder X-Ray Diffraction (Mo-PXRD)

Operando PXRD data were collected on a Bruker D8 A25 powder diffractometer with Mo radiation (0.7093 λ), focusing mirror optics and a Dectris Eiger 500R 2D detector with panoramic Soller slits. The detector position and opening were fixed to cover a 2θ range from 2° to 21°. The capillaries were mounted with both ends open and fixed to a flow cell (1 mm outer diameter) attached to a Leister Le Mini heat gun and connected to the gases with Swagelok connections. The heat gun nozzle position was used to align the capillary in the X-ray beam with the help of a double laser alignment system. The catalyst was pretreated following the same conditions described above. The catalytic reaction took place at atmospheric pressure and 400 °C with the catalyst powder pressed and sieved into 250–420 µm particles. The reactor had 8 mg of catalyst, with an approximated partial pressure of methanol (MeOH) of 130 mbar (lab temperature around 20 °C). The total flow was 3.5 ml/min (0.5 ml/min MeOH and 3 ml/min argon), giving a space velocity of 4.4 $g_{MeOH}/g_{catalyst}$ h. The effluent from the reactor was analyzed with an online Pfeiffer Omnistar quadrupole mass spectrometer. PXRD patterns were continuously recorded with 30 s exposure time plus another 30 s approximately between each measurement. The patterns were analyzed by parametric Rietveld refinement [20] using TOPAS [21] to extract the refined unit cell parameters (orthorhombic cell; *Pnnm* space group, "Ferrierite siliceous" from IZA database) [22], framework atom positions were fixed, and the coke occupancy as a function of time-on-stream (TOS). In order to account for the residual electron density in the zeolite channels dummy carbon atoms were added into the H-Ferrierite framework. The selected model was obtained by studying difference Fourier maps of the fully deactivated sample. It counts with 7 dummy atoms, 5 of them are in *ab* plane in the intersection between 8 and 10T channels, the other 2 are in the middle of 8T channel right in the *ac* plane.

3 Results and Discussion

3.1 Deactivation of H-Ferrierite Catalyst

The catalyst was provided by Zeolyst International (CP914C) with a silicon to aluminium ratio of 10. Accelerated deactivation conditions were applied: WHSV = 2 $g_{MeOH}/g_{catalyst}$ h, 307 mbar partial pressure of methanol and a reaction temperature of 400 °C. Due to the used conditions the conversion of methanol to hydrocarbons rapidly drops and shows a very sharp activity peak around 1 h on stream (Fig. 2a). Negligible conversion to hydrocarbons was observed after 2 h on stream (See Fig. 2). Since the time resolution of the GC–MS is 62.5 min for good separation of aromatic species, two experiments with a 25 min delay were performed, and the data were combined (Fig. 2a). In order to obtain spent catalysts at different stages of deactivation two catalytic tests were stopped after 43 and 56 min respectively.

This dramatically fast deactivation profile contrasted with the slow induction process where even after nearly 1 h on stream, full conversion was not yet achieved. However, it should be emphasized that the total yield of gas phase products detected by the FID (total detector count) at that point implied that the methanol conversion products were mainly retained in the porous material (Fig. S1). During this induction period, the hydrocarbon pool is built and methanol mainly reacts with the retained active species predominantly forming bigger polyaromatic structures of coke. This hypothesis is also in agreement with the observed hydrocarbon selectivity on either site of the maximum activity peak (Fig. 2b). During these first minutes we observe very few aromatics and/or higher aliphatic in the gas phase. The most common gas phase products are methane, C_2 and C_3. The formation of methane, which is hydrogen rich, is easily

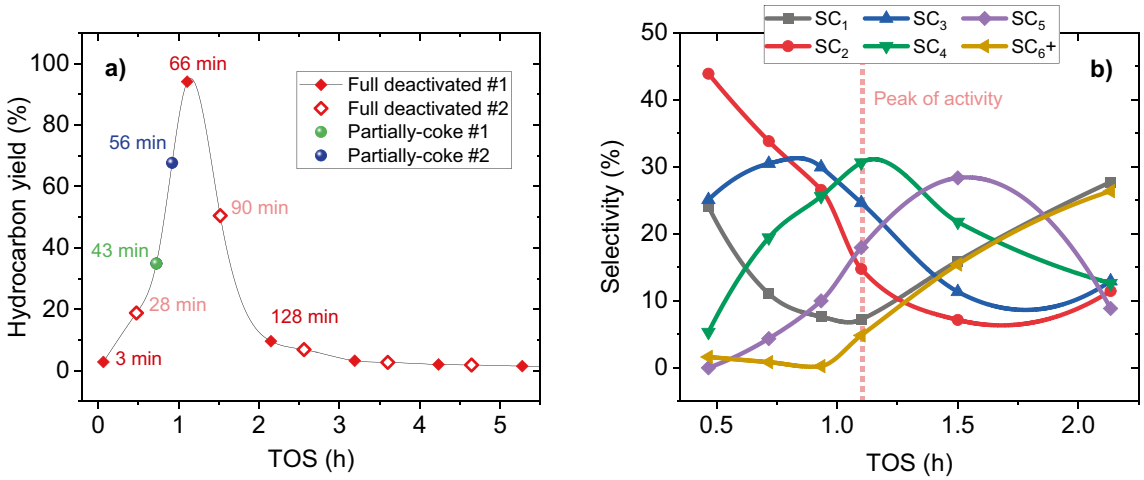

Fig. 2 Evolution with time on stream of the **a** total hydrocarbon yield (in C units) and **b** hydrocarbon selectivity for the MTH reaction to different components with certain carbon number over H-Ferrerite zeolite. Conditions: 400 °C, 307 mbar of MeOH, 2 g_{MeOH}/g_{cat} h. Color code used across the whole document is as follows: green ■ partially coked (43 min), blue ■ partially coked (56 min) and red ■ fully coked

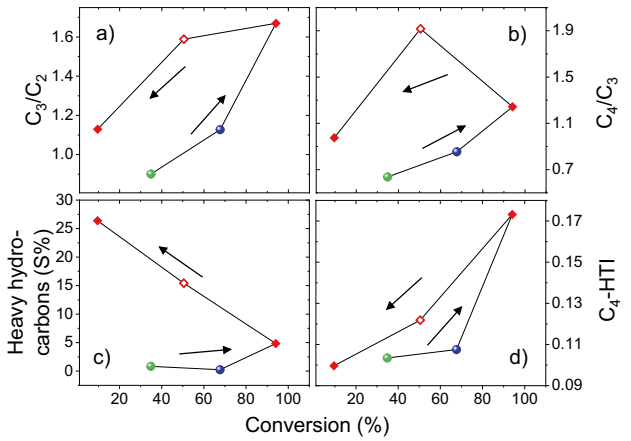

Fig. 3 Evolution with conversion level of **a** C_3/C_2 ratio, **b** C_4/C_3 ratio, **c** heavy hydrocarbons lumped (all aromatic products and C_6 or more combined) selectivity and C_4 hydrogen transfer index. C_4-HTI is calculated as the ratio between butanes and butenes. Color code used across the whole document is as follows: green ■ partially coked (43 min), blue ■ partially coked (56 min) and red ■ fully coked

reconcilable with appreciable coking and buildup of the hydrocarbon pool, consisting of hydrogen poor species [23]. The presence of C_2, and C_3 in the gas phase at this point indicates product formation from the aromatics cycle [24]. Check Figs. S2 and S3 for raw chromatograms of relevant time stamps.

The process progressively evolves into heavier fractions in a cascade fashion. The selectivity to C_3 reaches the maximum later but few minutes before the full activity peak when the catalyst is more selective to C_4 (Fig. 2b). In the minutes between full activity and deactivation, we observe a dramatic change in product ratios (Fig. 3a, b) as a consequence of the hydrocarbon distribution in Fig. 2b. While the maximum of C_3/C_2 ratio is observed at full methanol conversion (1.6 in Fig. 3a), a C_4/C_3 ratio maximum of 1.9 is reached when the catalyst is partially deactivated, suggesting a change in the dominant paths of the MTH reaction mechanism [24, 25].

After the activity peak, C_5 selectivity reached a maxima before complete deactivation where most of hydrocarbons are C_1 and heavy hydrocarbons (Fig. 3c). The increased selectivity towards higher aliphatics is then caused by loss of cracking activity with deactivation, as observed previously for ZSM-22 [26]. Hydrogen transfer reactions were monitored with C_4 hydrogen transfer index (C_4-HTI), calculated as the C_4 alkanes/alkenes ratio. They occur in parallel to intermediates cyclization, and eventually aromatic formation and condensation to coke. As an experimental descriptor for deactivation. The C_4-HTI which never reached 0.17, is relatively low at all times (Fig. 3d), due to insufficient space inside the H-Ferrierite channels [15]. Presumably, methane, is the major hydrogen acceptor in this rapidly deactivating system. It is clear that the maximum value of this index is observed at the highest conversion, with these secondary reactions being attenuated with coking.

To further study this behavior, intermediate deactivated samples were collected after 43 and 56 min on stream, before full conversion activity. The feed stream was switched to inert and cooled down to room temperature. These samples, along with fresh and fully deactivated catalysts, were characterized by N_2 adsorption–desorption and TGA (Fig. 4). N_2 adsorption–desorption isotherms are near type I isotherm in all cases, with the fresh catalyst partially or totally losing the micropores (adsorption at very low relative pressure) after partial (after 43 min or 56 min of reaction) or full

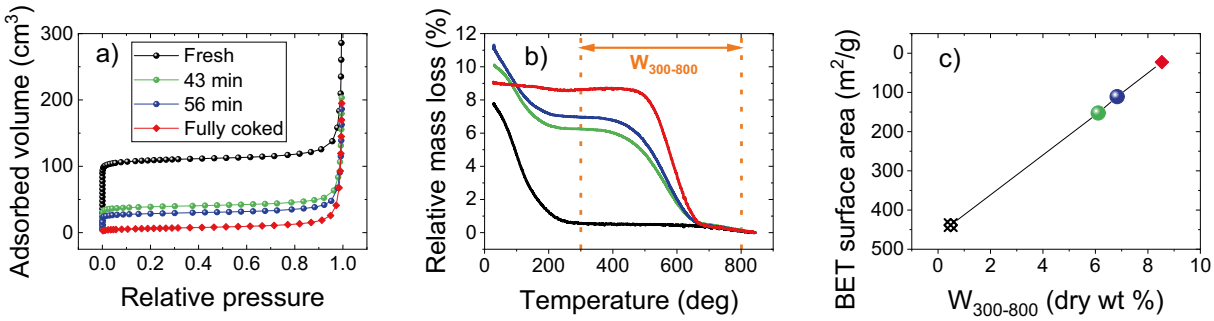

Fig. 4 Effect of deactivation degree on **a** N_2 adsorption isotherms and **b** TGA profiles normalized to the final relative mass loss. **c** Correlation between the observed amount of coke ($W_{300\text{-}800}$) and BET surface area. Color code used across the whole document is as follows: black ■ fresh catalyst, green ■ partially coked (43 min), blue ■ partially coked (56 min) and red ■ fully coked

deactivation (Fig. 4a). The fresh catalyst had BET surface area of 438 m^2/g, which is comparable to the value given by the provider; 400 m^2/g.

The TGA curves (Fig. 4b) are plotted in mass percentage (Relative mass loss %) and they are normalized to the calcined values, i.e.; 800 °C. The amount of coke is calculated as weight percent over the dry catalyst (dry wt %), it is the difference between 300 and 800 °C ($W_{300\text{-}800}$, vertical dotted lines). While the water contents are the variation from room temperature to 300 °C. The values of $W_{300\text{-}800}$ follow the expected trend; ≈ 0% the fresh catalyst, ≈ 6%, ≈ 7% and ≈ 8%, for partially coked samples and fully coked respectively. The correlation between the BET surface area reduction and the coking degree of the samples is outstanding (Fig. 4c). Nonetheless, the coking degree is already remarkable even after only 43 min TOS where the induction period is still at early stage. This however can be explained by the different state of the catalyst at the reaction (400 °C under a reactant stream) and characterization conditions (room and liquid nitrogen temperature). Therefore, while the activity of the catalyst is still increasing in the induction period, active hydrocarbon pool species can be measured by TGA as trapped species inside the pores.

3.2 X-Ray Diffraction

The X-Ray diffraction patterns of the two extreme cases (fresh and deactivated) are shown for clarity in Fig. 5a. The main differences between the diffractograms of the 4 samples consist of decreasing intensity of the first reflection (Fig. 5b) and peak shifting towards low angle (Fig. 5c). Such observations already suggested increases of lattice parameters and electron density inside the channels, giving a hint of what kind of descriptor could be appropriate.

Rietveld refinements of the four samples were performed with *Pnnm* space group because *Immm* model failed in quantifying coke's electron density accurately. The maximum symmetry model resulted in unassigned electron density around the bridging oxygen between rigid layers, further supporting the absence of straight T-0-T bridging bonds [3]. For the series of data analysis; atomic positions of the framework and dummy atoms are fixed, all T atoms are modelled

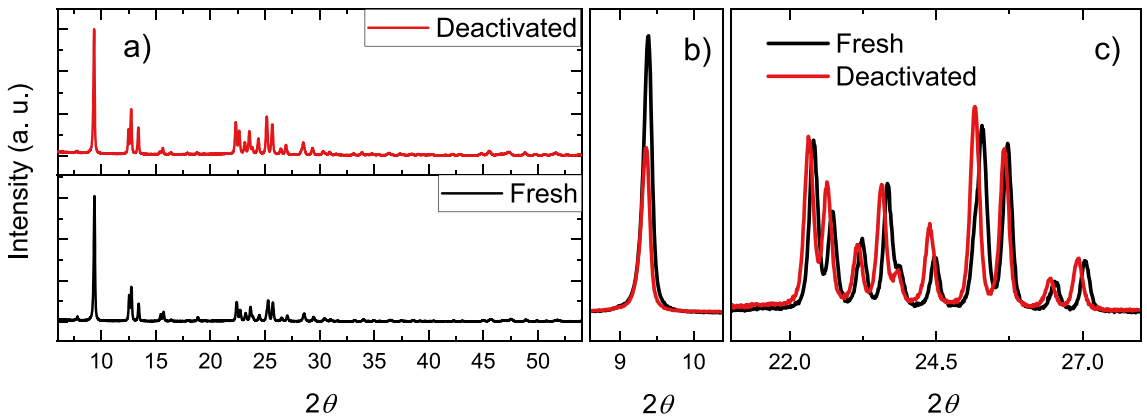

Fig. 5 **a** X-Ray diffraction pattern of fresh (black) and fully deactivated (red) H-Ferrerite and zoomed key regions in **b** from 8 to 11 and **c** from 21 to 28 2θ respectively ($\lambda_{(Cu)} = 1.5406$ Å)

as silicon and the refinement parameters are lattice parameters, dummy C occupancies and thermal parameters of Si, O and C.

3.3 Structural Effect of Deactivation

The three lattice parameters showed a slight increase with coking; *a* has the most significant enlargement, ≈ 0.07 Å, representing 0.5% extension compared to the fresh sample, followed by *c* ≈ 0.066 Å (0.35%) and finally *b,* which expanded only ≈ 0.015 Å (0.2%). The values of lattice parameters for all refinement are listed in Table S1, whereas the total unit cell volumes (*U. cell vol.*) are detailed in Table 1 for dry and hydrated samples. The values of unit cell volume increased from 1972.6 to 1993.6 $Å^3$ ≈ 1%. This occurs gradually as deactivation progresses, and it is the first XRD descriptor that can be used for H-Ferrierite.

The dummy atoms in the model provide a reasonably accurate estimation of the coke content independently. Occupancies of the carbon atoms are free parameters during the refinement but their positions are not refined (viewing of these positions in Fig. S5). These dummy atoms do not represent actual carbon atoms but serve as placeholders for residual electron density attributed to coke, hydration or any other impurity found inside the pores. Hereby, the second XRD based descriptor investigated is the effective coke content; *Non Framework Species Mass,* (*NFSM %*). The dummy atom occupancies can be translated into an effective coke content measure with the following formula:

$$NFSM\ \% = \frac{M_C \sum_i C_i}{36M_{Si} + 72M_O + M_C \sum_i C_i}.100$$

where M_C, M_{Si} and M_O are the respective molecular weights and *Ci* is the occupancy of the individual 1–7 dummy atoms (Refer to atoms coordinate and multiplicity list in Table S2). *NFSM %* should be carefully interpreted since it is sensitive to any molecules inside the channels and all this electron density is assigned to carbon atoms. However, it is a very useful simplification giving a semi-quantitative idea of the actual coke content of dry samples ($W_{300\text{-}800}$) without the need for secondary calibration, which is necessary in the case of the *U. cell vol*. The main advantage of the latter is that *U. cell vol.* is not significantly affected by water content (see Table 1), therefore it gives an estimate of deactivation level without the need to take much care with ambient moisture. Examples of Rietveld fits are plotted in the supporting information, Fig. S6.

Table 1 XRD descriptors (*U. cell vol.* and *Non framework species mass*, *NFSM %*) derived from the fitting of Fresh, partially and fully deactivated H-Ferrerite samples compared to the observed coke by thermogravimetric analysis

SAMPLE	*U. cell vol.* ($Å^3$)	*NFSM (%)*	Condition	$W_{300\text{-}800}$ TGA
Fresh catalyst	1972.6	1.2	Dry	0.5
	1972.5	7.0	Hydrated	
43 min TOS	1987	5.4	Dry	6.1
	1987.9	6.2	Hydrated	
56 min TOS	1990.9	6.7	Dry	6.8
	1991.3	6.8	Hydrated	
Fully coked	1993.6	8.2	Dry	8.5
	1994	8.4	Hydrated	

A comparison between the *NFSM %* predicted by the model and the obtained experimental coke content ($W_{300\text{-}800}$) is shown in Table 1. Moreover, Fig. 6 shows relationships between the model descriptors and experimental coke contents and BET surface area values. Both show a nice linear trend that suggests that both descriptor can successfully track catalyst deactivation even at early stages of the MTH reaction.

3.4 *Operando* Catalytic Testing

Due to the potential mismatch between the statuses of ex-situ samples with the real catalyst conditions the *operando* experiment was performed (See Fig. S7 for a picture depicting the set up). The evolution of the two proposed descriptors was monitored during in situ MTH experiments to test their accuracy to follow deactivation at real experiment conditions due to trapped hydrocarbon species. Exemplary diffractograms are shown in the Fig. S8 of the Supporting Information. The main MS signals corresponding to methanol (31), propene (41) and DME (45) were followed online. Diffractograms (30 s) were taken every minute approximately. Figure 7 shows the evolution with TOS of the two XRD descriptors and the recorded MS signals. Catalyst deactivation was faster in this case due to the higher space velocity required in the operando setup. Propene maximum, as a control signal of hydrocarbons, is reached after ca. 10 min on stream. Comparing the *NFSM %* values, an asymptotic value at ca. 4% is observed for *operando* measurement. Nevertheless, values up to 8.5% were observed in ex-situ measurement, confirming the expected difference between both and the extra expansion of the lattice observed when hydrocarbon species are cooled down within the zeolite pores, influenced by the well-known negative thermal expansion of FER [27] but also perhaps an extra condensation of light hydrocarbons. It is important to highlight that the reaction conditions of the reactor for ex-situ samples and the flow cell for *operando* are significantly different.

Immediately after methanol feed started *NFSM %* rapidly grew, as this descriptor accounts for all electron density inside the pores. Otherwise, the *U. cell vol.* required almost 10 min to reach comparable distortion values. This

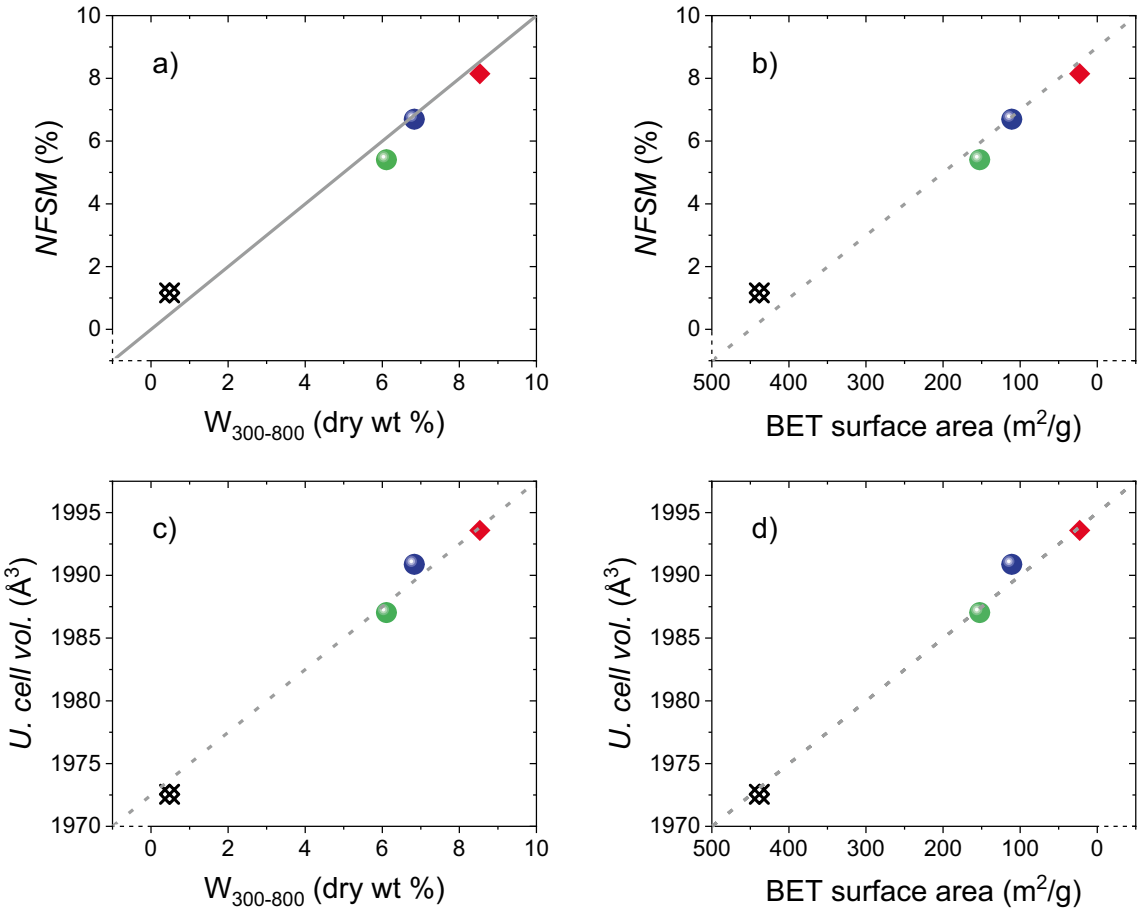

Fig. 6 Relationships between: *NFSM %* **a** with coke content in dry basis ($W_{300-800}$) where the parity line is plotted as solid gray line and **b** with BET surface area; *U. cell vol.* with **c** coke and **d** BET area respectively where predicted linear trends are shown for clarity. Color code used across the whole document is as follows: black ■ fresh catalyst, green ■ partially coked (43 min), blue ■ partially coked (56 min) and red ■ fully coked

could be interpreted as an early formation of hydrocarbon pool species that do not distort the lattice parameters but are recognized by the *NFSM %* descriptor. As soon as big polymethylbenzenes are formed, aromatic rings pressured the pore network enough to be detected. The values of the descriptors are ca. 2% and 1964 when propene maximum is observed, which is an indicator of the maxima hydrocarbon yields (Fig. 2a). At that point, ex-situ indicators already predicted an almost full distorted lattice. During the *operando* experiment, both descriptors keep increasing until a substantial deactivation is observed from the MeOH signal of the MS, where actually bigger hydrocarbon blocks exist at reaction conditions. These bigger species lead to the pore blockage and catalysts deactivation (drop of propene signal in the MS).

The peak in the MS signal for DME well before maximum catalytic activity probably reflects the high conversion of methanol to DME during the induction period. Only a small increase in the unit cell volume is seen at this point, despite the *NFSM %* sharp increasing. See the residuals evolution vs time plot at Fig. S9, where the higher residuals are actually before the methanol feed started, reinforcing the points from the experiment modeling. Therefore, this suggests that filling the pores to with small molecules like DME or light alkenes does not cause much expansion, although the electron density in the channels is measurable.

4 Conclusions

The evolution of methanol-to-hydrocarbon (MTH) active and deactivating species trapped within the zeolite pores has been monitored by ex-situ and *operando* X-Ray diffraction (XRD). H-Ferrerite has been selected as specific catalytic system that allows to follow the induction and deactivation periods of a zeolite in reasonable lab-scale equipment. Since the two gradient-coked samples were actually tests stopped during the induction period, before the activity reached the

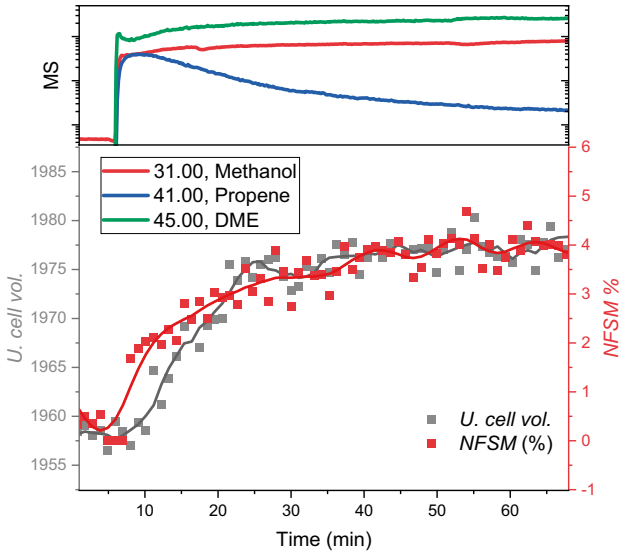

Fig. 7 *Operando* deactivation of H-Ferrierite at 400 °C, 130 mbar of MeOH, 4.4 g_{MeOH}/g_{cat} h. MS signals of methanol (31), propene (41) & DME (45) are plotted in the top. Time-resolved evolution of XRD descriptors shown in the bottom where a smooth line is also plotted for clarity

100% conversion. Our ex-situ results suggest that most of the intermediate MTH species that deform the lattice of the zeolite are formed during the induction period.

Our PXRD structural studies of H-Ferrierite suggest two easily extracted descriptors; *Non Framework Species Mass %*, and the unit cell volume. Those descriptors derived from ex-situ measurements were correlated with the experimental evidence of coking; observed through TGA and N_2 adsorption–desorption characterization. A direct linear trend was observed between both descriptors and the measured coke content and BET surface area. Unit cell volume is notably unaffected by hydration of the sample and by the presence of small molecules during the early stages of the induction period.

In-house *operando* PXRD allowed a better understanding of lattice parameters behavior during the induction and deactivation periods. A short initial period with a maximum yield of DME and very little distortion of the zeolite lattice suggested that the species produced early in the reaction are not big enough to distort the pore network significantly. Then, the growth of aromatic intermediates results in an increase of the *U. cell vol.* similar to what was observed in ex-situ experiments. Nevertheless, the higher sensitivity of the descriptors at operando conditions matched better the distortion of the lattice due to coke species formation with the rate of catalyst deactivation. The apparent mismatch between ex-situ and *operando* coking rates could be justified by the dramatically different experimental conditions of the tests and/or by extra condensation of light hydrocarbons upon cooling when the lattice parameters will naturally relax back to bigger values due to negative thermal expansion, however in order to prove this, extra experiments will be performed in the future.

5 Supporting Information Description

Total carbon in the FID detector, Raw GC data, SEM pictures of the commercial FER sample, visual of the dummy atom model used with the suggested structure, examples of Rietveld refinements, picture of the flow cell with a sketch depicting the *operando* set up, an example of the resolution in the *operando* experiment, evolution of residuals vs time, summary table of all refined parameters of the ex-situ study and a table containing all atomic coordinates of our model.

Supplementary Information The online version contains supplementary material available at https://doi.org/10.1007/s11244-023-01780-0.

Acknowledgements The Research Council of Norway is acknowledged for the support via TomoCAT researcher project (Project no. 301619). We also acknowledge the use of the Norwegian national infrastructure for X-ray diffraction and scattering (RECX).

Author Contributions The manuscript was written through contributions of all authors. All authors have given approval to the final version of the manuscript.

Funding Open access funding provided by University of Oslo (incl Oslo University Hospital).

Declarations

Competing interest The authors declare no competing financial interest.

References

1. Xu H, Zhu J, Zhu L, Zhou E, Shen C (2020) Advances in the synthesis of ferrierite zeolite. Molecules 25(16):3722. https://doi.org/10.3390/molecules25163722
2. Gramlich-Meier R, Gramlich V, Meier WM (1985) The crystal structure of the monoclinic variety of ferrierite. Am Miner 70(5–6):619–623

3. Alberti AASC (1987) Statistical and true symmetry of ferrierite: possible absence of straight T-O-T bridging bonds. Z Kristallogr 178:249–256
4. Bonilla A, Baudouin D, Pérez-Ramírez J (2009) Desilication of ferrierite zeolite for porosity generation and improved effectiveness in polyethylene pyrolysis. J Catal 265(2):170–180. https://doi.org/10.1016/j.jcat.2009.04.022
5. Bastiani R, Lam YL, Henriques CA, da Silva Teixeira V (2013) Application of ferrierite zeolite in high-olefin catalytic cracking. Fuel 107:680–687. https://doi.org/10.1016/j.fuel.2012.11.009
6. Catizzone E, Daele SV, Bianco M, Di Michele A, Aloise A, Migliori M, Valtchev V, Giordano G (2019) Catalytic application of ferrierite nanocrystals in vapour-phase dehydration of methanol to dimethyl ether. Appl Catal B 243:273–282. https://doi.org/10.1016/j.apcatb.2018.10.060
7. Lee Y, Park MB, Kim PS, Vicente A, Fernandez C, Nam I-S, Hong SB (2013) Synthesis and catalytic behavior of ferrierite zeolite nanoneedles. ACS Catal 3(4):617–621. https://doi.org/10.1021/cs400025s
8. Hu H, Ke M, Zhang K, Liu Q, Yu P, Liu Y, Li C, Liu W (2017) Designing ferrierite-based catalysts with improved properties for skeletal isomerization of n-butene to isobutene. RSC Adv 7(50):31535–31543. https://doi.org/10.1039/C7RA04777K.DOI:10.1039/C7RA04777K
9. Dai H, Lee C, Liu W, Yang T, Claret J, Zou X, Dauenhauer PJ, Li X, Rimer JD (2022) Enhanced selectivity and stability of finned ferrierite catalysts in butene isomerization. Angew Chem Int Ed 61(8):e202113077. https://doi.org/10.1002/anie.202113077
10. Khivantsev K, Wei X, Kovarik L, Jaegers NR, Walter ED, Tran P, Wang Y, Szanyi J (2022) Palladium/ferrierite versus palladium/SSZ-13 passive NOx adsorbers: adsorbate-controlled location of atomically dispersed palladium(ii) in ferrierite determines high activity and stability**. Angew Chem Int Ed 61(3):e202107554. https://doi.org/10.1002/anie.202107554
11. Hamon C, Malefant K, Neveu B (2007) Catalyst based on ferrierite/iron for catalytic reduction of nitrous oxide content in gases, method for obtaining same and application. France
12. Tao L, Lee I, Khare R, Jentys A, Fulton JL, Sanchez-Sanchez M, Lercher JA (2022) Speciation of Cu-Oxo clusters in ferrierite for selective oxidation of methane to methanol. Chem Mater 34(10):4355–4363. https://doi.org/10.1021/acs.chemmater.1c04249
13. Haw JF, Song W, Marcus DM, Nicholas JB (2003) The mechanism of methanol to hydrocarbon catalysis. Acc Chem Res 36(5):317–326. https://doi.org/10.1021/ar020006o
14. Olsbye U, Svelle S, Lillerud KP, Wei ZH, Chen YY, Li JF, Wang JG, Fan WB (2015) The formation and degradation of active species during methanol conversion over protonated zeotype catalysts. Chem Soc Rev 44(20):7155–7176. https://doi.org/10.1039/C5CS00304K.DOI:10.1039/C5CS00304K
15. Qi L, Li J, Xu L, Liu Z (2016) Evolution of the reaction mechanism during the MTH induction period over the 2-dimensional FER zeolite. RSC Adv 6(61):56698–56704. https://doi.org/10.1039/C6RA09237C.DOI:10.1039/C6RA09237C
16. Rojo-Gama D, Nielsen M, Wragg DS, Dyballa M, Holzinger J, Falsig H, Lundegaard LF, Beato P, Brogaard RY, Lillerud KP et al (2017) A Straightforward descriptor for the deactivation of zeolite catalyst H-ZSM-5. ACS Catal 7(12):8235–8246. https://doi.org/10.1021/acscatal.7b02193
17. Rojo-Gama D, Mentel L, Kalantzopoulos GN, Pappas DK, Dovgaliuk I, Olsbye U, Lillerud KP, Beato P, Lundegaard LF, Wragg DS et al (2018) Deactivation of zeolite catalyst H-ZSM-5 during conversion of methanol to gasoline: operando time- and space-resolved X-ray diffraction. J Phys Chem Lett 9(6):1324–1328. https://doi.org/10.1021/acs.jpclett.8b00094
18. Wragg DS, O'Brien MG, Bleken FL, Di Michiel M, Olsbye U, Fjellvåg H (2012) Watching the methanol-to-olefin process with time- and space-resolved high-energy Operando X-ray diffraction. Angew Chem Int Ed 51(32):7956–7959. https://doi.org/10.1002/anie.201203462
19. Wragg D, Svelle S, Lundegaard LF, Beato P. Crystallography as a tool for studying methanol conversion in zeolites. In: Miguel A, Bañares IW (eds) Springer handbook of advanced catalyst characterization. Springer, New York
20. Stinton GW, Evans JSO (2007) Parametric Rietveld refinement. J Appl Crystallogr 40(1):87–95. https://doi.org/10.1107/S0021889806043275
21. Coelho A (2018) TOPAS and TOPAS-academic: an optimization program integrating computer algebra and crystallographic objects written in C++. J Appl Crystallogr 51(1):210–218. https://doi.org/10.1107/S1600576718000183
22. Morris RE, Weigel SJ, Henson NJ, Bull LM, Janicke MT, Chmelka BF, Cheetham AK (1994) A synchrotron X-ray diffraction, neutron diffraction, 29Si MAS-NMR, and computational study of the siliceous form of zeolite ferrierite. J Am Chem Soc 116(26):11849–11855. https://doi.org/10.1021/ja00105a027
23. Schulz H (2010) "Coking" of zeolites during methanol conversion: basic reactions of the MTO- MTP- and MTG processes. Catal Today 154(3):183–194. https://doi.org/10.1016/j.cattod.2010.05.012
24. Bjørgen M, Svelle S, Joensen F, Nerlov J, Kolboe S, Bonino F, Palumbo L, Bordiga S, Olsbye U (2007) Conversion of methanol to hydrocarbons over zeolite H-ZSM-5: on the origin of the olefinic species. J Catal 249(2):195–207. https://doi.org/10.1016/j.jcat.2007.04.006
25. Svelle S, Joensen F, Nerlov J, Olsbye U, Lillerud K-P, Kolboe S, Bjørgen M (2006) Conversion of methanol into hydrocarbons over Zeolite H-ZSM-5: ethene formation is mechanistically separated from the formation of higher alkenes. J Am Chem Soc 128(46):14770–14771. https://doi.org/10.1021/ja065810a
26. Teketel S, Svelle S, Lillerud K-P, Olsbye U (2009) Shape-selective conversion of methanol to hydrocarbons over 10-ring unidirectional-channel acidic H-ZSM-22. ChemCatChem 1(1):78–81. https://doi.org/10.1002/cctc.200900057
27. Bull I, Lightfoot P, Villaescusa LA, Bull LM, Gover RKB, Evans JSO, Morris RE (2003) An X-ray diffraction and MAS NMR study of the thermal expansion properties of calcined siliceous ferrierite. J Am Chem Soc 125(14):4342–4349. https://doi.org/10.1021/ja0292400